

4-8-2015

# Using time-frequency analysis to determine time-resolved detonation velocity with microwave interferometry

David E. Kittell  
*Purdue University*

Jesus O. Mares  
*Purdue University*

Steven F. Son  
*Purdue University*

Follow this and additional works at: [https://docs.lib.purdue.edu/perc\\_articles](https://docs.lib.purdue.edu/perc_articles)

---

## Recommended Citation

D. E. Kittell, J. O. Mares Jr., and S. F. Son, "Using time-frequency analysis to determine time-resolved detonation velocity with microwave interferometry," *Rev. Sci. Instrum.* 86(4), 044705 (2015). <http://dx.doi.org/10.1063/1.4916733>

This document has been made available through Purdue e-Pubs, a service of the Purdue University Libraries. Please contact [epubs@purdue.edu](mailto:epubs@purdue.edu) for additional information.

# Using time-frequency analysis to determine time-resolved detonation velocity with microwave interferometry

David E. Kittell, Jesus O. Mares, and Steven F. Son

Citation: *Review of Scientific Instruments* **86**, 044705 (2015);

View online: <https://doi.org/10.1063/1.4916733>

View Table of Contents: <http://aip.scitation.org/toc/rsi/86/4>

Published by the *American Institute of Physics*

---

## Articles you may be interested in

[A hybrid dielectrophoretic system for trapping of microorganisms from water](#)

*Biomicrofluidics* **9**, 034110 (2015); 10.1063/1.4922276

[2D IR spectroscopy reveals the role of water in the binding of channel-blocking drugs to the influenza M2 channel](#)

*The Journal of Chemical Physics* **140**, 235105 (2014); 10.1063/1.4881188

[Pressure-driven variations of hydrogen bonding energy in ammonium azide \(NH<sub>4</sub>N<sub>3</sub>\): IR absorption and Raman scattering studies](#)

*The Journal of Chemical Physics* **141**, 024703 (2014); 10.1063/1.4886184

[Molecular interactions at the hexadecane/water interface in the presence of surfactants studied with second harmonic generation](#)

*The Journal of Chemical Physics* **142**, 224704 (2015); 10.1063/1.4922304

[Origin of the Hadži ABC structure: An ab initio study](#)

*The Journal of Chemical Physics* **143**, 184305 (2015); 10.1063/1.4935062

[Phase diagram of ammonium perchlorate: Raman spectroscopic constrains at high pressures and temperatures](#)

*The Journal of Chemical Physics* **144**, 244701 (2016); 10.1063/1.4953909

---



# Using time-frequency analysis to determine time-resolved detonation velocity with microwave interferometry

David E. Kittell, Jesus O. Mares, Jr., and Steven F. Son  
*Purdue University, West Lafayette, Indiana 47907, USA*

(Received 24 August 2014; accepted 22 March 2015; published online 8 April 2015)

Two time-frequency analysis methods based on the short-time Fourier transform (STFT) and continuous wavelet transform (CWT) were used to determine time-resolved detonation velocities with microwave interferometry (MI). The results were directly compared to well-established analysis techniques consisting of a peak-picking routine as well as a phase unwrapping method (i.e., quadrature analysis). The comparison is conducted on experimental data consisting of transient detonation phenomena observed in triaminotrinitrobenzene and ammonium nitrate-urea explosives, representing high and low quality MI signals, respectively. Time-frequency analysis proved much more capable of extracting useful and highly resolved velocity information from low quality signals than the phase unwrapping and peak-picking methods. Additionally, control of the time-frequency methods is mainly constrained to a single parameter which allows for a highly unbiased analysis method to extract velocity information. In contrast, the phase unwrapping technique introduces user based variability while the peak-picking technique does not achieve a highly resolved velocity result. Both STFT and CWT methods are proposed as improved additions to the analysis methods applied to MI detonation experiments, and may be useful in similar applications. © 2015 AIP Publishing LLC. [<http://dx.doi.org/10.1063/1.4916733>]

## I. INTRODUCTION

Microwave interferometry (MI) is an established technique to measure shock and detonation velocities in explosives. This technique is used to measure the phase and amplitude of microwave signals that are transmitted through an unreacted explosive and reflected back at locations of interest. These reflection points are located at dielectric discontinuities such as a shock wave or a reaction front<sup>1,2</sup> which occur in the media during a detonation event. The phase measurements can then be used to infer the relative position and velocity of the phenomena. MI is a unique non-intrusive diagnostic for explosives research with high temporal resolution; however, challenges exist due to transmission losses and partial reflection of the signal.

Achievable MI signals in explosives are often of a low quality, and velocity measurements in non-ideal systems remain challenging. Total reflection of the MI signal is never realized due to partial transmission through the wave front of interest,<sup>2</sup> as well as attenuation of the signal due to absorption and dispersion effects in the explosive media.<sup>3</sup> Furthermore, the shock or detonation wave may be a non-planar reflector due to sample diameter effects as well as material heterogeneities<sup>4</sup> resulting in poor signal quality. Other factors which may affect the signal quality include the possibility of a decoupled shock-reaction zone (e.g., shock initiation and detonation failure) giving rise to multiple harmonic frequencies,<sup>1</sup> as well as the confinement of the test explosive acting as a waveguide for the MI signal.<sup>3</sup> When several of these non-idealities are present simultaneously, it may still be possible to extract useful velocity information with an advanced time-frequency analysis.

Despite ongoing research since the early 1950's<sup>3</sup> and subsequent improvements made to microwave interferometers,<sup>5-7</sup> the explosives' community has been slow to apply time-frequency analysis for velocity measurements. Originally, a simple peak picking or zero crossing method was used to determine the average velocity at finite points in time. Although much of the information contained in the MI signal is lost, this technique can be effective for variable amplitude signals, or when aggressive filtering is needed to determine a phase angle. Modern interferometers now employ two-channel output for phase unwrapping and continuous position measurement. Current phase unwrapping techniques attempt to account for all non-idealities in low quality signals at the expense of possibly introducing error through heavy filtering, normalization, and smoothing of the data.<sup>6</sup> Velocity is then numerically derived from position-time data, resulting in additional numerical errors and requiring additional filtering. The effort required to perform phase unwrapping is highly dependent on the quality of the MI signal, and it is possible that subtle transient features in velocity may be obscured after the application of heavy filtering.

Time-frequency analysis is established in other fields of interferometry including photonic Doppler velocimetry (PDV)<sup>8,9</sup> and velocity interferometer system for any reflector (VISAR).<sup>10</sup> These analysis techniques hold several advantages for MI over phase unwrapping, including the direct measurement of velocity through frequency (and not by a numerical derivative), robust data analysis for low quality signals, and minimal filter settings with less potential for user bias. Two of the most widely used analysis methods are the short-time Fourier transform (STFT) and the continuous wavelet transform (CWT).

In this work, the objective is to explore both time-frequency methods and phase unwrapping using two cases of experimental data. A direct comparison is then made between all three techniques for high and low quality MI signals. Overall, the challenges of analyzing MI signals in explosives are unique from other interferometry techniques such as PDV and VISAR due to significant non-idealities commonly present in explosive media.

## II. EXPERIMENTAL METHODS

A 35 GHz signal was generated using a custom microwave interferometer<sup>11</sup> and transmitted to the test article through a solid 0.635 cm diameter polytetrafluoroethylene (PTFE) waveguide. A quadrature mixer was used to produce two-channel output 90° out of phase and was recorded at 2.5 GHz using a Tektronix DPO4034 digital phosphor oscilloscope. The MI output was de-sampled to 100 MHz for data analysis, and the highest frequency content of the output signal was below 4 MHz. Timing of the experiment was based on first light observed by fiber optics: an M34L02 Thorlab patch cable with a 600  $\mu\text{m}$  core diameter transmitted light to a DET10A Thorlab photodetector with 1 ns rise time. The detonation event was contained inside a thick-walled steel box; a schematic of the experiment is shown in Fig. 1.

In this study, high explosives were pressed into 0.652 cm I.D. 304 stainless steel tubes for velocity measurement. A Teledyne Risi, Inc., RP-502 detonator was used to initiate a detonation in a booster explosive, which transitioned into the test article. The booster consisted of Primasheet 1000, and the test article consisted of either pressed triaminotrinitrobenzene (TATB) powder or a stoichiometric mixture of ammonium nitrate and urea (ANUR). Material properties of the explosives are summarized in Table I, including the Chapman-Jouguet detonation velocity and sample length. The average material wavelength values for Primasheet 1000 and TATB were determined from the Landau-Lifschitz/Looyenga (LLL) mixture equation<sup>1</sup> and previous work.<sup>11</sup> The average wavelength for ANUR was estimated for the analysis because no previous data or mixture laws exist for this material at MI frequencies.

## III. ANALYSIS TECHNIQUES

Four different methods are discussed to analyze the two-channel MI output. With each technique, a common set of data analysis procedures was identified and is summarized here. The pre-treatment of the signal consisted of a low-pass filter to eliminate high-frequency noise, and the signal was cropped from the initiation of the booster to the end of the test article. A scaled time variable,  $\hat{t}$ , was introduced to account for the discontinuous jump in velocity at  $t = 0$ ; it is defined by the piecewise equation,

$$\hat{t} = \begin{cases} (2/\lambda_1)t & : t \leq 0 \\ (2/\lambda_2)t & : t > 0 \end{cases}, \quad (1)$$

where  $\lambda_1$  and  $\lambda_2$  correspond to the material wavelength of the booster and test article, respectively. Equation (1) was used to eliminate the material wavelength from the velocity equations, as the time-varying frequency content of the signal is proportional to velocity with a scale factor of unity in the  $\hat{t}$ -domain. The MI signal in the  $\hat{t}$ -domain was re-sampled to a common sampling rate limited by the equation

$$V_S = \frac{1}{2} F_S \times \min(\lambda_1, \lambda_2), \quad (2)$$

where  $F_S$  is the original sampling frequency and  $V_S$  is the maximum achievable sampling rate over the entire scaled time signal.

The analysis methods consist of discrete peak-picking, phase unwrapping (i.e., quadrature analysis), and time-frequency ridge extraction using both STFT and CWT operations. A complete discussion of the short-time Fourier transform and continuous wavelet transform is beyond the scope of the work, therefore only basic theory and equations are presented; the interested reader is referred to other sources.<sup>12–14</sup>

### A. Peak-picking analysis

Peak-picking is a discrete method to determine the average detonation velocity at a finite number of points. This method is unbiased from signal filtering, provided the filtering operations do not interfere with the identification of local maxima and minima in time. The analysis is derived from the

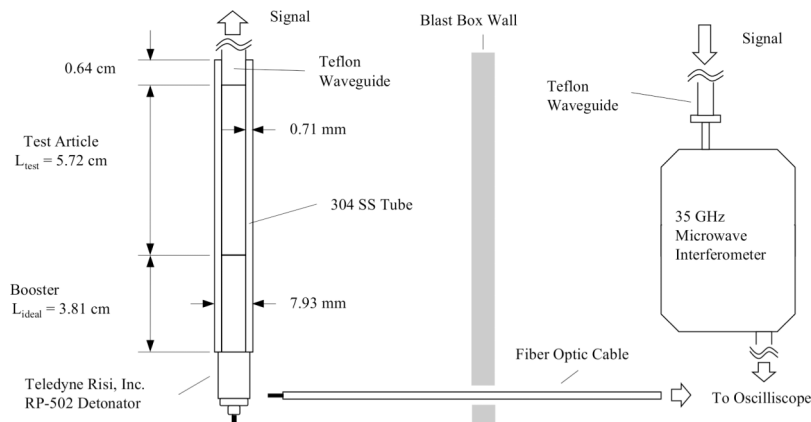


FIG. 1. Schematic drawing of the microwave interferometer and test article (not to scale).

TABLE I. Material properties of the explosives used for study.

Explosive	$\rho_{ave}$ (g/cm <sup>3</sup> )	$\lambda$ (mm)	D <sub>CJ</sub> (mm/ $\mu$ s)	$L_{ex}$ (cm)
Primasheet 1000	1.50	5.67	7.1	3.81
TATB	1.538	5.08	6.8	5.72
ANUR	1.08	5.0	5.5	5.72

fundamental velocity-frequency relationship,<sup>1</sup>

$$v(t) = \frac{\lambda_k}{2} f(t), \quad (3)$$

where  $f(t)$  is the time-varying frequency content of the MI signal, and  $\lambda_k$  is the calibrated material wavelength corresponding to an explosive,  $k$ , in a multi-material system ( $k > 1$ ). The material wavelength is dependent on microwave frequency, sample diameter, and permittivity; values of  $\lambda_k$  used in this work are shown in Table I. To calculate velocity from the MI output, each advance in phase of the signal by  $2\pi$  corresponds to the advance of the moving reflector by  $\lambda_k/2$  and the time between consecutive peaks. Thus, an average time-velocity series may be constructed between the  $i$ th and  $(i + 1)$ th peaks as

$$\left( \frac{t_{i+1} + t_i}{2}, \frac{\lambda_k/2}{t_{i+1} - t_i} \right), \quad (4)$$

which is a discretization of Eq. (3). The resolution of this method could be improved using time points from minima, maxima, and zero crossings; however, the most reliable calculations are made between similar features (e.g., peak-to-peak). A simple automated routine was used to identify the local minima and maxima, and the discrete velocity calculations are presented with the results.

## B. Quadrature analysis

Quadrature analysis, or phase unwrapping, provides greater spatial resolution than discrete peak-picking. The objective of this analysis is to calculate a phase angle from the two-channel MI output using circularized Lissajous curves; however, the MI signals must be filtered, normalized, and transformed. Initially, low-pass filters are used to eliminate most of the high frequency noise from the signal. For time-varying signals, especially those corresponding to significant variation in velocity (e.g., detonation failure), filters are applied in multiple sections for a range of frequencies. The resulting signals are then spliced together and filtered to eliminate higher frequency noise. A linear map is then used to normalize the microwave signals between extrema to the interval  $[-1, 1]$ .

After normalization, the Lissajous curves lie on an ellipse and will introduce measurement error. The correction of this quadrature fringe measurement error is discussed in detail in previous work.<sup>15</sup> Here, the equation of an ellipse is written in terms of the phase angle,  $\theta$ , as

$$\vec{f}(\theta) = \vec{Z} + Q \cdot \begin{bmatrix} A \times \cos(\theta) \\ B \times \sin(\theta) \end{bmatrix}, \quad (5)$$

where  $Q$  is the rotation matrix about an angle,  $\alpha$ , and  $A$ ,  $B$ ,  $\vec{Z}$  are the fitted parameters. For the normalized Lissajous curves, Eq. (5) is fitted with a non-linear least squares regression using the Bookstein constraint.<sup>16</sup> Equation (5) may be rearranged to solve for the transformed MI signals  $V_1'$  and  $V_2'$ ,

$$\begin{bmatrix} V_1' \\ V_2' \end{bmatrix} = \begin{bmatrix} \frac{1}{A} & 0 \\ 0 & \frac{1}{B} \end{bmatrix} \cdot Q^T \cdot \left( \begin{bmatrix} V_1 \\ V_2 \end{bmatrix} - \begin{bmatrix} Z_1 \\ Z_2 \end{bmatrix} \right), \quad (6)$$

where  $V_1$  and  $V_2$  are the normalized signals, and the phase angle may then be calculated as

$$\theta = \tan^{-1} \left( \frac{V_2'}{V_1'} \right), \quad (7)$$

where  $\tan^{-1}$  is the discontinuous arctangent function effectively unwrapping the phase.

Finally, detonation velocity is calculated with a numerical derivative of the phase angle

$$v(t) = \frac{\lambda_k}{4\pi} \frac{d\theta}{dt}. \quad (8)$$

As discussed in Sec. III, the scaled time variable defined in Eq. (1) may be used to eliminate the material wavelength,  $\lambda_k$ , from the velocity expression to obtain

$$v(\hat{t}) = \frac{1}{2\pi} \frac{d\theta}{d\hat{t}}, \quad (9)$$

where Eq. (9) provides a continuous transition in velocity from the booster to the test explosive.

A numerical derivative for variable time-step is required to calculate the velocity appearing in Eq. (9). While multiple methods exist,<sup>11,17</sup> a discrete formula was chosen based on the work of Savitzky and Golay,<sup>18</sup>

$$f'(x^*) \approx \sum_{k=1}^3 2kc_k \frac{f_k - f_{-k}}{x_k - x_{-k}}, \quad (10)$$

where the coefficients are  $c_1 = 5/32$ ,  $c_2 = 4/32$ , and  $c_3 = 1/32$ , and  $k$  is the index about the point where the derivative is evaluated ( $k = 0$ ). An additional low-pass filter is applied to compute a final velocity.

## C. Short-time Fourier transform

The windowed Fourier transform, or STFT, is defined for a time-varying signal  $f(t)$  by

$$STFT[f(\tau, \omega)] = \int_{-\infty}^{\infty} f(t) w(t - \tau) e^{-i\omega t} dt, \quad (11)$$

where  $w(t)$  is a windowing function,  $\tau$  is the integration variable, and  $\omega$  is the angular frequency. For this work, a Hamming windowing function was chosen, and the window width was held constant as a percentage of the total signal length. The accuracy and precision limitations of a windowed Fourier transform are discussed in other work pertaining to PDV measurements.<sup>19,20</sup>

Time-frequency bin sizes for the STFT are determined from the sampling frequency and the period of the signal

according to the relations

$$\Delta t = 1/F_S \quad (12a)$$

and

$$\Delta f = 1/T, \quad (12b)$$

where  $F_S$  is the sampling frequency and  $T$  is the period, or total length, of the signal. To ensure time-frequency bin sizes of  $0.01 \mu\text{s}$  and  $0.01 \text{ MHz}$ , the MI signals were zero padded to extend the signal to a period of  $T = 100 \mu\text{s}$  before applying the STFT.

Detonation velocity is found by extracting the amplitude ridge line of the spectrogram. Here, the ridge line is determined by the maximum spectrogram amplitude at each value in time. Once a suitable window width is determined, the scaled time variable  $\hat{t}$  from Eq. (1) is passed to the STFT so that the spectrogram frequency is directly proportional to velocity with a scale factor of unity.

#### D. Continuous wavelet transform

Formally, the CWT of a time-varying signal  $f(t)$  is given by<sup>21</sup>

$$Wf(u, s) = \int_{-\infty}^{\infty} f(\xi) \frac{1}{\sqrt{s}} \psi^* \left( \frac{\xi - u}{s} \right) d\xi, \quad (13)$$

where  $Wf$  denotes the wavelet transform,  $u$  and  $s$  are the translation and scale variables,  $\xi$  is the integration variable,  $\psi$  is the mother wavelet, and  $\psi^*$  denotes its complex conjugate. Scale and translation are related to time and frequency through the choice of the mother wavelet. In Eq. (13), the function  $\psi$  should satisfy the admissibility condition<sup>21</sup> and have a zero mean value.

Following previous work,<sup>8–10,12</sup> a Gabor mother wavelet was chosen as the basis for the CWT and is given by the formula

$$\psi(t) = \frac{1}{(\sigma^2\pi)^{1/4}} e^{-t^2/2\sigma^2} e^{i\eta t}, \quad (14)$$

where  $\sigma$  and  $\eta$  are the time spread and center frequency parameters. For the Gabor mother wavelet, time and frequency can be related to scale and translation via<sup>22</sup>

$$t = u \quad (15a)$$

and

$$\omega = \eta/s. \quad (15b)$$

Kim and Kim<sup>12</sup> show that the Gabor wavelet shape is controlled by a single dimensionless parameter and introduce the notation of a Gabor wavelet shaping factor  $Gs = \sigma\eta$ , where  $\sigma$  is set to unity. The shaping factor  $Gs$  governs the time-frequency resolution of the CWT according to the relations<sup>23</sup>

$$\sigma_{t_{u,s}} = \frac{Gs}{\sqrt{2}\omega} \quad (16a)$$

and

$$\sigma_{\omega_{u,s}} = \frac{\omega}{\sqrt{2}Gs}, \quad (16b)$$

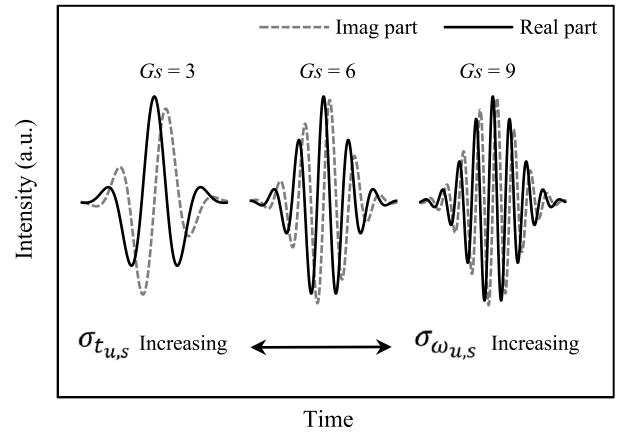


FIG. 2. Gabor mother wavelet  $\psi(t)$  for  $Gs$  of 3, 6, and 9.

where  $\sigma_{t_{u,s}}$  and  $\sigma_{\omega_{u,s}}$  are the variances (or spread) in time and frequency of the CWT. The effect of  $Gs$  on the Gabor wavelet shape is depicted in Fig. 2.

The relative weighting on time or frequency resolution is determined by the number of oscillations in the Gabor wavelet shape; in the limit  $Gs \rightarrow \infty$ , the GWT becomes similar to a time-independent FFT. In the limit  $Gs \rightarrow 0$ , the number of oscillations decreases to improve time localization; however, this also introduces error due to frequency spreading. When  $Gs = 0$ , the Gabor wavelet collapses to a normal distribution and violates the admissibility condition (zero mean value). In general, the Gabor wavelet has a non-zero mean; however, it is suggested that  $Gs \geq 3$  is sufficient to minimize the mean such that the conditions for a mother wavelet are satisfied.<sup>22,24</sup> Consequently, a frequency bias is introduced near  $Gs = 3$  and was corrected following other work.<sup>25</sup>

To visualize the time-frequency intensity, a normalized scalogram is calculated in place of a spectrogram according to the formula<sup>22</sup>

$$N_W f(u, s) = \frac{|Wf(u, s)|^2}{s}. \quad (17)$$

Values of  $s$  may be calculated at will via Eq. (15b) so that any discretization of frequency may be transformed into an array of scale values and passed to the CWT. Hence, the desired frequency bin size may be achieved without zero padding.

Unlike the STFT window width, the  $Gs$  parameter is restricted to a small range of values between 3 and 5.5.<sup>22</sup> It is bounded from below by the admissibility condition, and from above by acceptable temporal resolution. To motivate the upper limit, Eqs. (16a) and (16b) are combined

$$\frac{\sigma_{t_{u,s}}}{T} = \frac{Gs}{2\sqrt{2}\pi}, \quad (18)$$

where  $T$  is the period at a particular frequency of the signal, and  $\sigma_{t_{u,s}}$  is the acceptable time spread. Therefore, to resolve transient phenomena occurring over a time interval on the order of one period, Eq. (18) implies that small  $Gs$  values  $\lesssim 9$  are needed. A fixed  $Gs$  value between 3 and 5 was also used in similar work.<sup>24</sup> The same ridge extraction algorithm and scaled time variable from the STFT method are used to produce the final normalized scalogram and velocity result.

TABLE II. Summary of the MI output and data analysis.

Test article	S/N	$t_i$ ( $\mu$ s)	$t_f$ ( $\mu$ s)	N	w (%)	$G_s$
TATB	140	-5.45	8.1	1355	0.5	4
ANUR	2.2	-6.0	60.0	6600	4.0	4

#### IV. RESULTS AND DISCUSSION

An assessment of the different analysis techniques was made using MI data for two trials with TATB and ANUR. These trials are representative of a wide range of detonation phenomena, as well as the non-idealities present in MI signals. For each trial, the average signal-to-noise ratio, number of samples, and parameters for the final time-frequency calculations are shown in Table II. In particular, the TATB data are of a higher quality ( $S/N = 140$ ) and are presented to illustrate that all methods are capable of determining a time-resolved detonation velocity. The ANUR data are of a lower quality ( $S/N = 2.2$ ) and are representative of the non-idealities in MI signals; the results clearly illustrate the benefits of using a time-frequency analysis over phase unwrapping techniques.

##### A. High quality signal

MI output obtained for the high quality TATB signal is shown in Fig. 3. For this trial, a detonation wave in the booster transitioned into the test article, which also detonated throughout its entire length; however, the detonation velocity was unsteady. The TATB explosive was pressed to an average volume fraction of  $V_A = 0.794$  in five increments, and density gradients were formed. The density gradients appear as oscillations in the velocity results due to the dependency of the detonation wave speed on material density.<sup>3</sup> This conclusion was also verified by changing the number of pressing intervals and observing a corresponding change in the number and amplitude of the oscillations in velocity.

Lissajous curves for the MI output and unwrapped phase angle are shown in Figs. 4 and 5, respectively. Despite a high signal-to-noise ratio, the initial Lissajous curve appears skewed and filled as a result of the non-constant

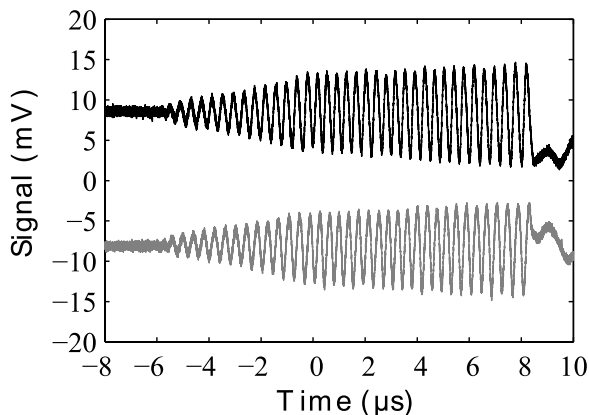


FIG. 3. Two-channel microwave output signals for TATB. Transition between TATB and booster occurs at  $t = 0$ .

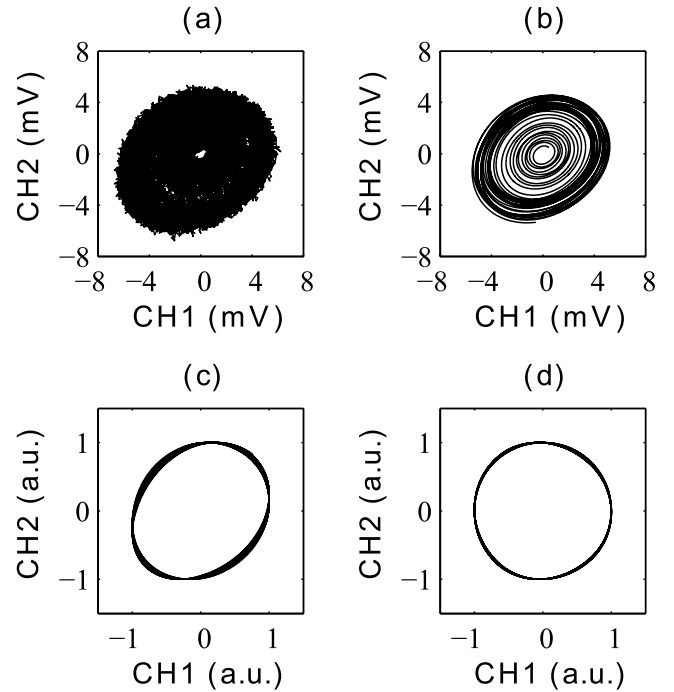


FIG. 4. Lissajous curves for sequential operations on TATB data. Clockwise from top left: (a) original, (b) filtered, (c) normalized, and (d) transformed.

amplitude; most of the signal inside the curve is of the booster explosive for  $t < 0$ . After filtering, normalization, and transformation, the final Lissajous curve is well circularized, and the unwrapped phase angle is presented in Fig. 5. The final velocity result is shown in Fig. 6 directly compared to the discrete velocity result from peak-picking (open circles). For the final filtering step of the quadrature analysis, filter settings were chosen to best fit between the discrete velocity data.

For an analysis of the TATB data using STFT, the MI signals were zero padded between  $-50 \mu$ s and  $50 \mu$ s, increasing the signal length from 1355 to 10 000 samples. Initially, the spectrogram was computed using four different window sizes as shown in Fig. 7. Because the frequency content of the signal is concentrated between 2 and 3 MHz, a single window size was capable of resolving the frequency ridge line. A final spectrogram in the time-modified  $\hat{t}$ -domain was computed using a window width  $w = 0.5\%$  of the signal

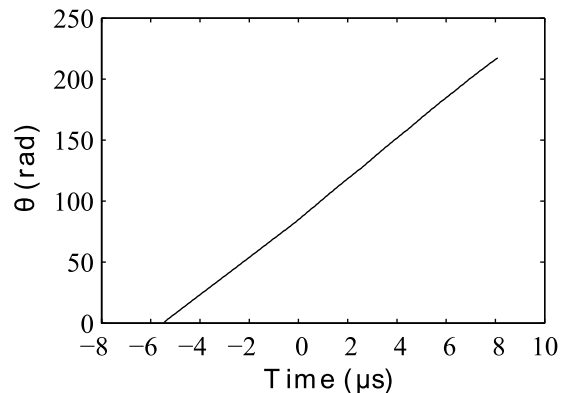


FIG. 5. Unwrapped phase angle from the quadrature analysis for TATB.

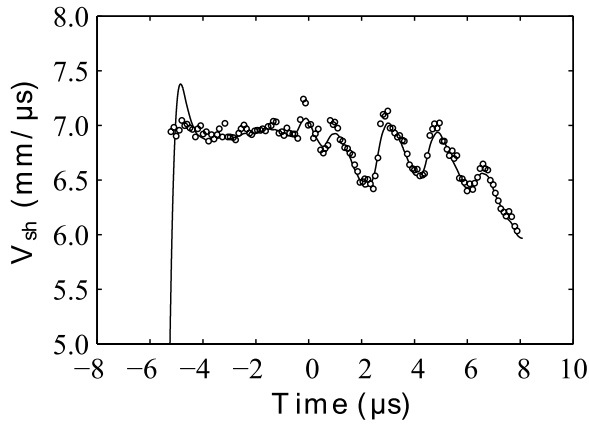


FIG. 6. Direct comparison of quadrature (solid line) and peak-picking (open circles) analyses for TATB data.

length, and the velocity result is shown in Fig. 8 in direct comparison with discrete peak-picking. The velocity result from STFT shows an excellent fit to the discrete calculations from peak-picking, as well as similarity with the quadrature analysis by extension.

Velocity calculations based on the CWT differ from the STFT approach due to the control of time-frequency resolution through the  $G_s$  parameter and not window width or signal length. The normalized scalogram was computed using  $G_s$  values within the range of 3–5.5<sup>22</sup> and is presented in Fig. 9. From the initial scalogram calculations, a fixed value of  $G_s = 4$  was selected. This value appears to be the minimum value (maximum temporal resolution) needed to resolve the MI signal and also satisfy the admissibility criteria. Although the frequency ridge lines in Fig. 9 contain more noise than the spectrogram ridge lines from STFT, the CWT is a noise-robust operation and the ridges may be filtered if desired. The final velocity calculation using the CWT-based method is shown in Fig. 10 with no filtering and the overlaid peak-picking calculations. The direct comparison of CWT and peak-picking velocity data confirms that both intersect, and that  $G_s = 4$  is a suitable choice for the Gabor wavelet shaping factor.

Quadrature analysis, STFT, and CWT-based methods are equally successful at fitting the discrete peak-picking velocity data for this trial. However, it is emphasized that the discrete velocity calculations from peak-picking were critical in the determination of filter settings for both the quadrature and STFT methods. Moreover, the local maxima and minima of

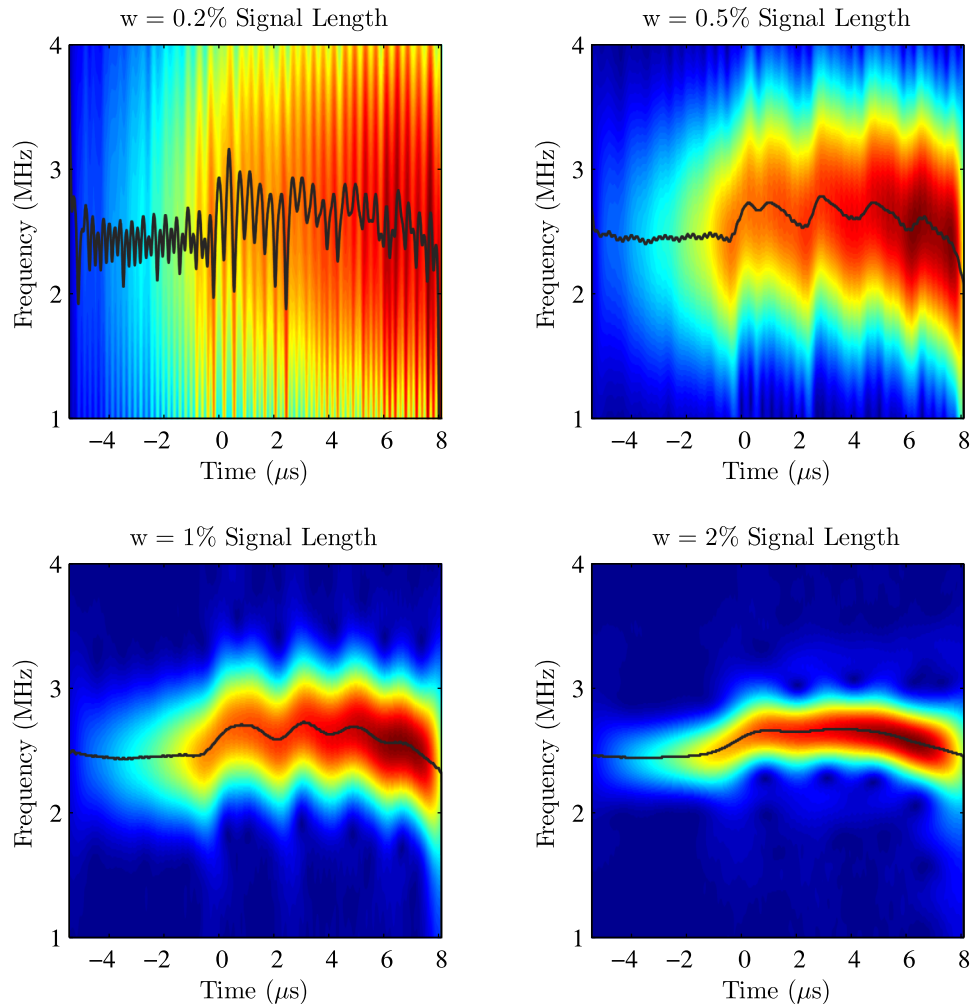


FIG. 7. Spectrogram of the MI signal for various window sizes,  $w$ , as a percentage of total signal length. Black solid lines indicate the maximum amplitude ridge.

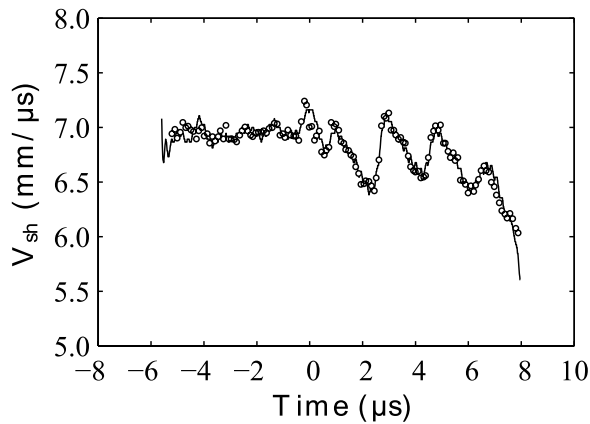


FIG. 8. Direct comparison of STFT (solid line) and peak-picking (open circles) analyses for TATB data.

the two-channel output occur with sufficient frequency so that the average velocity calculations are representative of the instantaneous time-resolved detonation velocity. In contrast, tuning of the  $G_s$  parameter for the CWT was independent of the velocity result from peak-picking; a value of  $G_s = 4$  may

be used for a vast number of time-frequency analyses without any knowledge of the desired result.

## B. Lower quality signal

MI output for the low quality signal corresponding to ANUR is shown in Fig. 11. For this trial, several non-ideal phenomena are observed, including the failure of detonation immediately following the transition of the booster into the test article. The detonation failure was confirmed by the partial recovery of the confiner material, as well as the wave speed existing well-below the Chapman-Jouguet detonation velocity for ANUR. In addition, the transmission of the MI signal is poor and the average signal-to-noise ratio of  $S/N = 2.2$  is difficult for analysis. A final complication is the exponential decay in the wave velocity, which spreads the relevant frequency content of the signal over the range of 0.1–2.5 MHz.

Lissajous curves for the MI signal are shown in Fig. 12 and do not resemble the previous trial. An electromagnetic pulse was captured near  $-10 \mu s$  due to the firing of an exploding bridge-wire detonator to initiate the booster explosive. However, the signal was cropped so that the pulse

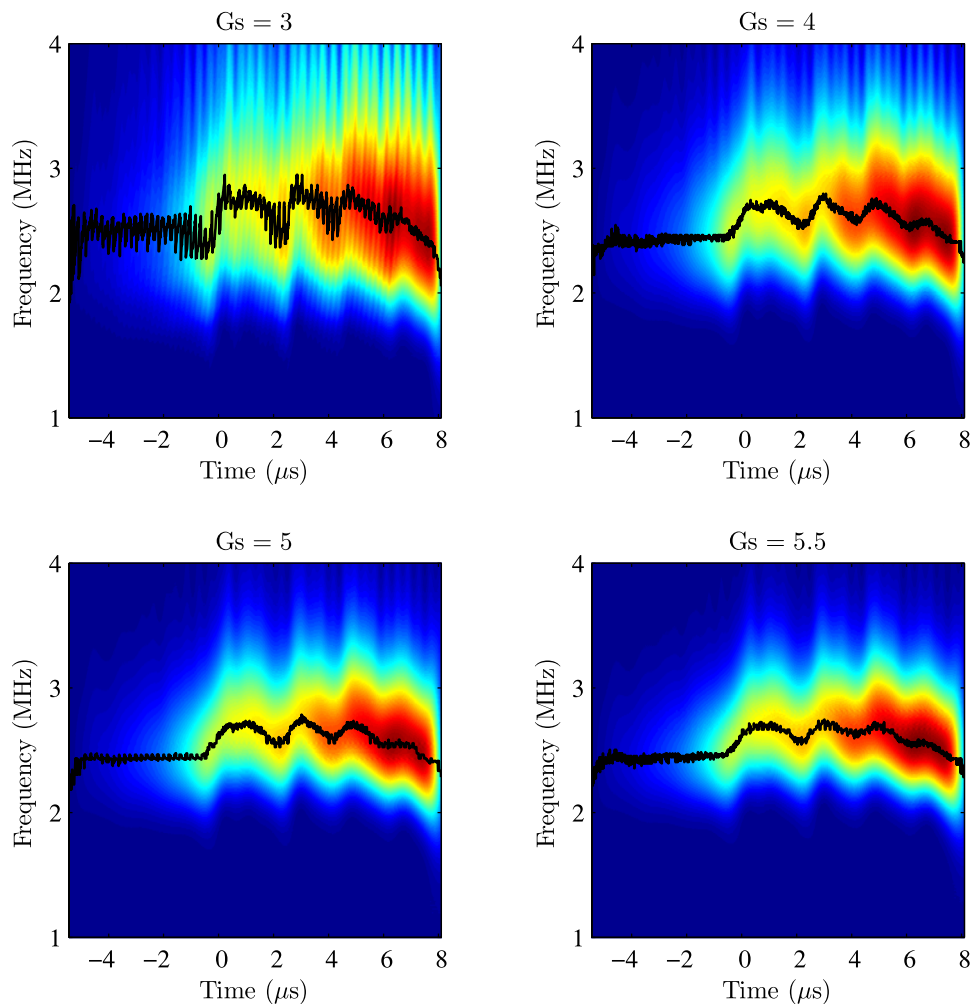


FIG. 9. Normalized scalogram of the MI signal for various values of the Gabor wavelet shaping factor,  $G_s$ . Black solid lines indicate the maximum amplitude ridge.

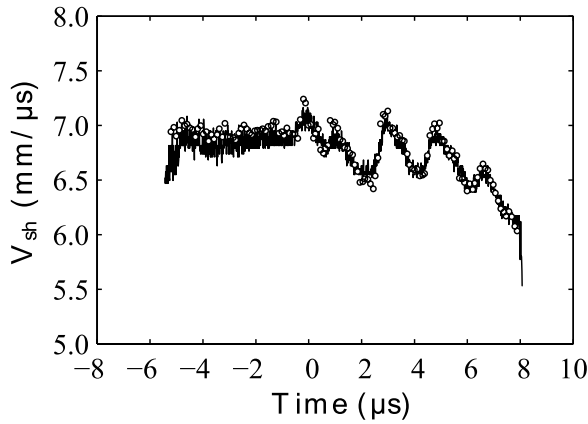


FIG. 10. Direct comparison of CWT (solid line) and peak-picking (open circles) analyses for TATB data.

does not appear in the Lissajous curves (refer to Table II). Despite the appearance of these data, quadrature analysis may still be used with considerable effort to unwrap the phase angle as shown in Fig. 13. The final velocity result presented in Fig. 14 fails to fully fit the discrete peak-picking result. Better agreement between quadrature analysis and peak-picking is achieved beyond 20  $\mu$ s; however, the transient event is not fully captured in the analysis.

Unlike quadrature analysis, the time-frequency methods appear to fit the discrete velocity calculations with less error, particularly near  $t = 0$ . Final STFT and CWT time-resolved detonation velocities are shown in Figs. 15 and 16, respectively, and are directly compared to the peak-picking analysis. One challenge unique to STFT is the determination of a suitable window width for the entire signal. For the chosen value of  $w = 4.0\%$  signal length, there is an excellent agreement between the discrete calculation for  $t > 0$ ; however, the higher velocity corresponding to the booster appears smeared in Fig. 15. A different window width may have been applied to the time interval  $t < 0$ ; instead, the window width was chosen to more closely fit the discrete calculations corresponding to the wave velocity in ANUR.

The potential advantage of a CWT-based analysis is illustrated by the time-resolved velocity calculations in Fig. 16. Not only does the CWT appear robust to noise for

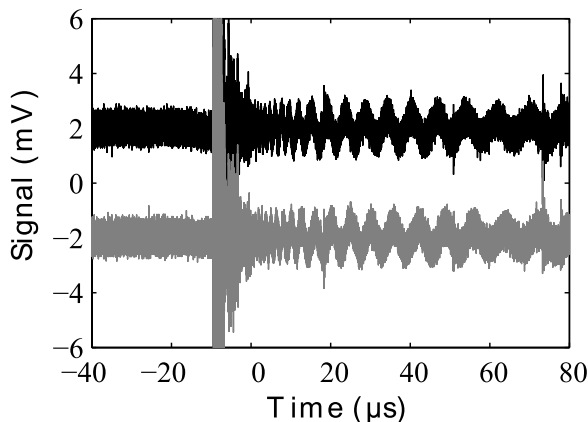


FIG. 11. Two-channel microwave output signals for ANUR. Transition between ANUR and booster occurs at  $t = 0$ .

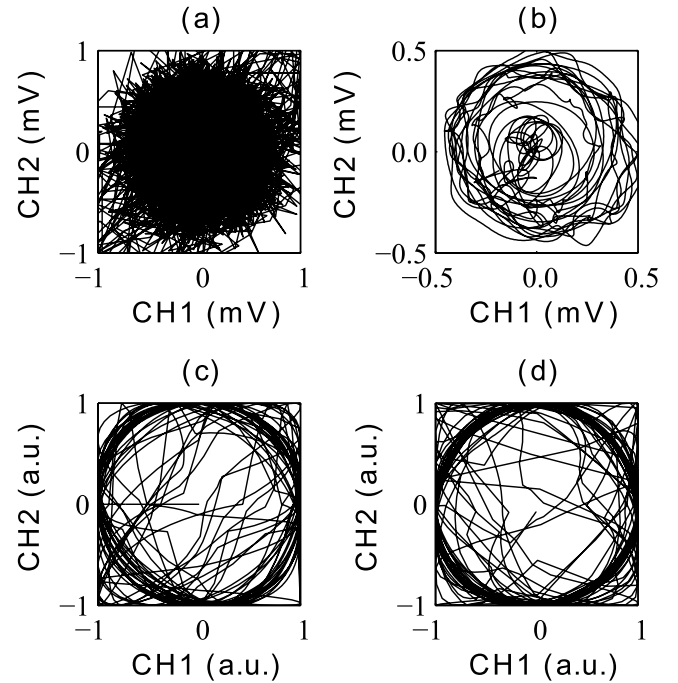


FIG. 12. Lissajous curves for sequential operations on ANUR data. Clockwise from top left: (a) original, (b) filtered, (c) normalized, and (d) transformed.

$S/N = 2.2$  but also the value  $G_s = 4$  achieves optimal time-frequency resolution required for a time-varying signal. This observation is significant because the same Gabor wavelet shaping factor was used in the previous trial; hence, no modification to the wavelet basis was required for the analysis of both signals presented in this work. Further, the ability to control the frequency bin size without the need for zero padding means that this method may be more computationally efficient than STFT-based calculations.

Overall, the effort required with phase unwrapping is highly dependent on the quality of the MI signal, and when several non-ideal effects are present, the results of this trial show significant advantages for using a time-frequency analysis. The Lissajous curves in Fig. 12 might possibly be improved with additional filtering and more advanced normalization techniques; however, additional effort and filter parameters are required. Even if a semi- or fully

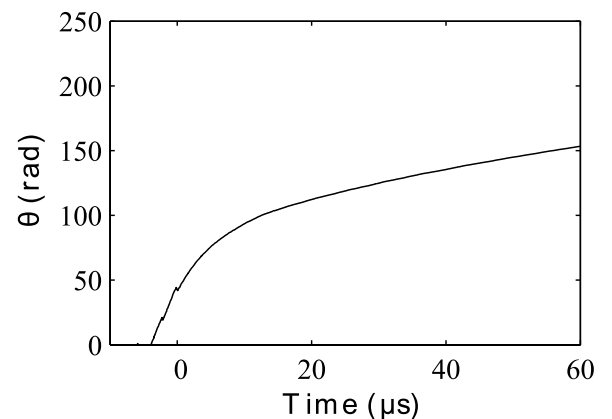


FIG. 13. Unwrapped phase angle from the quadrature analysis for ANUR.

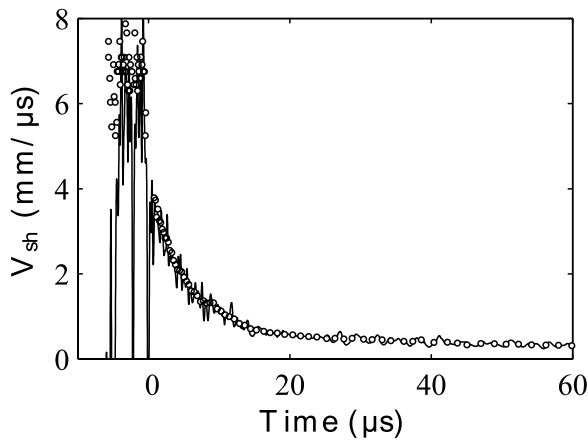


FIG. 14. Direct comparison of quadrature (solid line) and peak-picking (open circles) analyses for ANUR data.

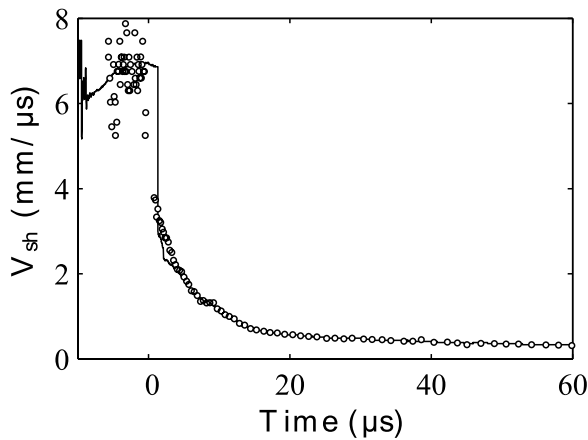


FIG. 15. Direct comparison of STFT (solid line) and peak-picking (open circles) analyses for ANUR data.

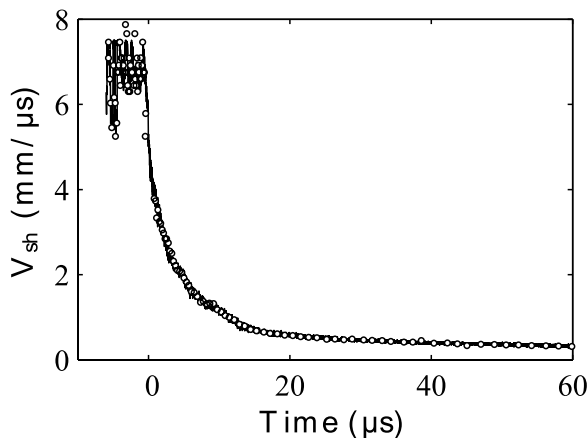


FIG. 16. Direct comparison of CWT (solid line) and peak-picking (open circles) analyses for ANUR data.

automated quadrature analysis is achieved, the STFT and CWT techniques may be implemented with a single filter parameter. The use of time-frequency analysis for MI yields a method with a single, bounded, filter parameter allowing for the standardization and reproducibility of detonation velocity measurements within the explosives community.

TABLE III. RMS values of the difference in velocity results; abbreviations are C (CWT), Q (quadrature), and S (STFT).

Signal	$t_i$ ( $\mu$ s)	$t_f$ ( $\mu$ s)	RMS value (mm/ $\mu$ s)		
			C-Q	C-S	S-Q
TATB	-5.1	8.0	0.13	0.11	0.12
ANUR	-3.9	60	0.69	0.42	0.93

### C. Deviations in velocity results

A direct comparison of quadrature, STFT, and CWT was made by calculating the root-mean-square (RMS) of the difference between velocity results. These values are summarized in Table III and show all the unique combinations of differences. For each calculation, the velocity results were cropped slightly to eliminate the influence of edge effects (refer to Table III). The RMS values show that velocity results from STFT and CWT are the most similar in both trials, whereas quadrature deviates from the time-frequency analyses. Additionally, RMS values for the high quality TATB signal are bounded between 0.11 and 0.13 mm/ $\mu$ s, which may suggest an estimate of the precision when using MI to determine a shock or detonation velocity. Finally, the RMS value is calculated over the entire velocity history, which penalizes deviations in the booster explosive. Although STFT and CWT are in excellent agreement for the low quality ANUR signal, errors in the ideal explosive ( $t < 0$ ) are reflected by the larger value of 0.42 mm/ $\mu$ s for this trial. Further work is needed to estimate the minimum error associated with each of these analysis techniques depending on the time scale, signal frequency, and noise content.<sup>19,20</sup>

### V. CONCLUSIONS

Time-frequency analysis methods based on STFT and CWT are used to determine the time-resolved detonation velocity with microwave interferometry. These methods are suggested as improved additions to the analysis tools currently used for MI, especially when several non-idealities are present during the observation of a detonation event. Velocity calculations are compared with established peak-picking and phase unwrapping (i.e., quadrature) techniques for two trials corresponding to examples of high and low quality MI signals. The higher quality signal illustrates that all methods are able to resolve the time-varying detonation velocity equally well under favorable conditions; however, minimal tuning of the CWT and STFT is required unlike quadrature analysis.

A low quality MI signal corresponding to an ANUR explosive was challenging to analyze with the quadrature method, and a time-frequency analysis was shown to be much more suitable. Of the two time-frequency methods proposed, the CWT-based analysis has a greater potential for the direct measurement of velocity. It is possible that a fixed Gabor wavelet shaping factor of  $G_s = 4$  may be used in all future calculations, as this value appears to be optimally adjusted for most time-varying MI signals. Therefore, minimal tuning of the wavelet basis is required as compared to the

variable windowing size for STFT. Both STFT and CWT methods are suggested as improved alternatives to quadrature analysis for determining a time-resolved detonation velocity. From the results of this work, time-frequency methods prove capable of resolving highly detailed detonation phenomena in non-idealized low quality MI signals. Additionally, a single, constrained parameter is used to control these analysis techniques and allows for minimal user bias in the extraction of velocity information from MI applied to explosives.

## ACKNOWLEDGMENTS

This material is based upon work supported by the U.S. Department of Homeland Security, Science and Technology Directorate, Office of University Programs, under Grant Award No. 2013-ST-061-ED0001. The views and conclusions contained in this document are those of the authors and should not be interpreted as necessarily representing the official policies, either expressed or implied, of the U.S. Department of Homeland Security.

<sup>1</sup>A. D. Krall, B. C. Glancy, and H. W. Sandusky, *J. Appl. Phys.* **74**, 6322 (1993).

<sup>2</sup>B. C. Glancy, H. W. Sandusky, and A. D. Krall, *J. Appl. Phys.* **74**, 6328 (1993).

<sup>3</sup>G. F. Cawsey, J. L. Farrands, and S. Thomas, *Proc. R. Soc. A* **248**, 499 (1958).

<sup>4</sup>S. I. Jackson, C. B. Kiyanda, and M. Short, *Proc. Combust. Inst.* **33**, 2219 (2011).

<sup>5</sup>L. D. Strand, A. L. Schultz, and G. K. Reedy, *J. Spacecr. Rockets* **11**, 75 (1974).

<sup>6</sup>G. H. McCall, W. L. Bongianni, and G. A. Miranda, *Rev. Sci. Instrum.* **56**, 1612 (1985).

<sup>7</sup>D. T. Foss, R. J. Roby, and W. F. O'Brien, *J. Propul. Power* **9**, 497 (1993).

<sup>8</sup>S. Liu, D. Wang, T. Li, G. Chen, Z. Li, and Q. Peng, *Rev. Sci. Instrum.* **82**, 023103 (2011).

<sup>9</sup>H. Song, X. Wu, C. Huang, Y. Wei, and X. Wang, *Rev. Sci. Instrum.* **83**, 073301 (2012).

<sup>10</sup>A. Sur, A. S. Rav, G. Pandey, K. D. Joshi, and S. C. Gupta, *IEEE International Conference on Advanced Electronic Systems (ICAES)* (IEEE, 2013), pp. 147–151.

<sup>11</sup>R. S. Janesheski, L. J. Groven, and S. F. Son, *Propellants, Explos., Pyrotech.* **39**, 609 (2014).

<sup>12</sup>Y. Y. Kim and E.-H. Kim, *J. Acoust. Soc. Am.* **110**, 86 (2001).

<sup>13</sup>C. Torrence and G. P. Compo, *Bull. Am. Meteorol. Soc.* **79**, 61 (1998).

<sup>14</sup>I. Daubechies, *IEEE Trans. Inf. Theory* **36**, 961 (1990).

<sup>15</sup>P. L. M. Heydemann, *Appl. Opt.* **20**, 3382 (1981).

<sup>16</sup>W. Gander, G. H. Golub, and R. Strebel, *BIT Numer. Math.* **34**, 558 (1994).

<sup>17</sup>R. D. Levie, S. Sarangapani, and P. Czekaj, *Anal. Chem.* **50**, 110 (1978).

<sup>18</sup>A. Savitzky and M. J. Golay, *Anal. Chem.* **36**, 1627 (1964).

<sup>19</sup>D. H. Dolan, *Rev. Sci. Instrum.* **81**, 053905 (2010).

<sup>20</sup>T. A. Ota, *Rev. Sci. Instrum.* **84**, 103906 (2013).

<sup>21</sup>S. Mallat, *A Wavelet Tour of Signal Processing*, 2nd ed. (Academic Press, New York, 1999).

<sup>22</sup>J.-C. Hong and Y. Y. Kim, *Exp. Mech.* **44**, 387 (2004).

<sup>23</sup>I. Simonovski and M. Boltežar, *J. Sound Vib.* **264**, 545 (2003).

<sup>24</sup>Y. Q. Deng, C. Wang, L. Chai, and Z. Zhang, *Appl. Phys. B* **81**, 1107 (2005).

<sup>25</sup>J. Slavič, I. Simonovski, and M. Boltežar, *J. Sound Vib.* **262**, 291 (2003).